Supplementary Information (SI) for ChemComm.

Supporting Information

Electric-field-promoted assembly of asymmetric junctions for single-molecule rectifiers

Yaqi Zhang,[a,b,c,+] Yaxuan Zhang,[b,c,+] Ting Pan,[b,c,+] Ping Zhou,[b,c] and Hongliang Chen[b,c,d,*]

[a] Department of Chemistry and Innovation Center of Pesticide Research, China Agricultural University, Beijing 100193, P. R. China

[b] Stoddart Institute of Molecular Science, Department of Chemistry, Zhejiang University, Hangzhou 310027, P. R. China

[c] ZJU-Hangzhou Global Scientific and Technological Innovation Center, Zhejiang University, Hangzhou 311215, P. R. China

[d] Beijing National Laboratory for Molecular Sciences, Beijing 100871, P. R. China

[+] These authors contributed equally

e-mail: hongliang.chen@zju.edu.cn

Table of Contents

Section A. Materials / Methods / Instruments 2

Section B. Synthesis procedures 2

Section C. NMR Spectroscopy 5

Section D. Supplemental STM-BJ Measurements 7

Section E. Theoretical calculations 14

Section F. Supplemental References 16

Section A. Materials / Methods / Instruments

Unless otherwise stated, all reagents were purchased from commercial suppliers and used without further purification. 1,2,4-trichlorobenzene (TCB) used for conductance measurements was obtained from Energy Chemical (anhydrous, 99.9%). Thin-layer chromatography (TLC) was performed using silica gel 60 F254 plates fro sm Merck. Column chromatography was conducted using a Biotage® Selekt system equipped with RediSep Rf Gold® normal-phase silica cartridges. Routine nuclear magnetic resonance (NMR) spectra were recorded on a Bruker Avance 600 MHz spectrometer, operating at 600 MHz for ^{1}H and 151 MHz for ^{13}C nuclei. Chemical shifts (*δ*) are reported in parts per million (ppm) relative to the residual non-deuterated solvent signals (DMSO-d_6: δ_H = 2.54 ppm, δ_C = 39.5 ppm; $CDCl_3$: δ_H = 7.26 ppm, δ_C = 77.2 ppm). High-resolution mass spectra (ESI-HRMS) were acquired on a Bruker timsTOF pro mass spectrometer.

Section B. Synthesis procedures

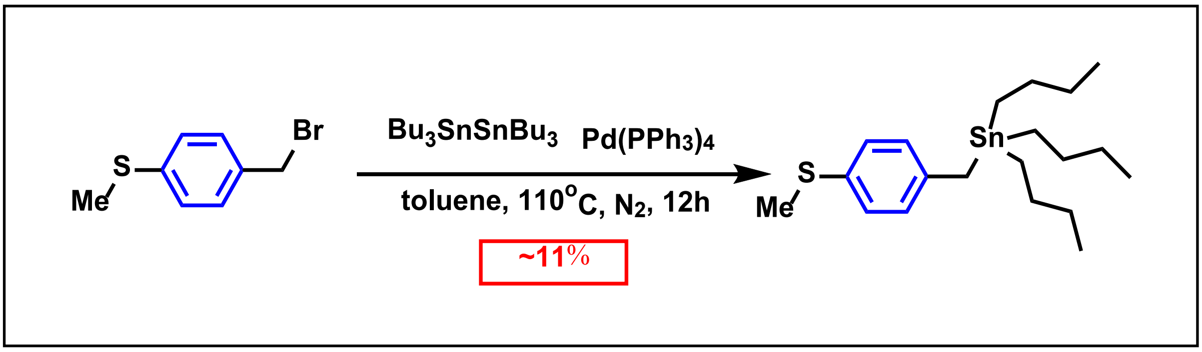

Scheme S1. Synthesis of **SMePhSn–1**.

SMePhSn–1: A 100 mL round-bottom flask, equipped with a magnetic stirrer, was charged with **(4-**(bromomethyl)phenyl)(methyl)sulfane (2.6 mmol, 1.0 equiv), $Bu_3SnSnBu_3$ (3.1 mmol, 1.2 equiv), $Pd(PPh_3)_4$ (0.26 mmol, 0.1 equiv), toluene (60 mL). The reaction mixture was stirred at 110 °C under an N_2 atmosphere for 12 h, cooled to room temperature, and passed through a pad of Celite. Then, 60 mL of water were added to the mixture and the solution extracted with

DCM (60 mL × 3). The combined organic layers were washed with brine, dried over Na_2SO_4 and evaporated *in vacuo*. The product was purified by silica gel chromatography using hexane as the eluent to give **SMePhSn–1** as a transparent liquid with a yield in ~11%. ^1H NMR (500 MHz, Chloroform-*d*) δ 7.06 (d, J = 8.2 Hz, 2H), 6.84 (d, J = 8.3 Hz, 2H), 2.37 (s, 3H), 2.19 (s, 2H), 1.39 – 1.30 (m, 6H), 1.19 (h, J = 7.3 Hz, 9H), 0.79 (t, J = 7.3 Hz, 9H), 0.76 – 0.70 (m, 6H). ^{13}C NMR (126 MHz, Chloroform-*d*) δ 140.5, 130.3, 127.2, 126.5, 28.1, 28.0, 27.9, 26.5, 26.3, 26.1, 16.7, 16.2, 12.7, 9.6, 8.3, 7.1. HRMS (MALDI-TOF) for **SMePhSn–1**; Calcd for $C_{20}H_{36}SSn$: m/z =428.1560; Found 428.1542.

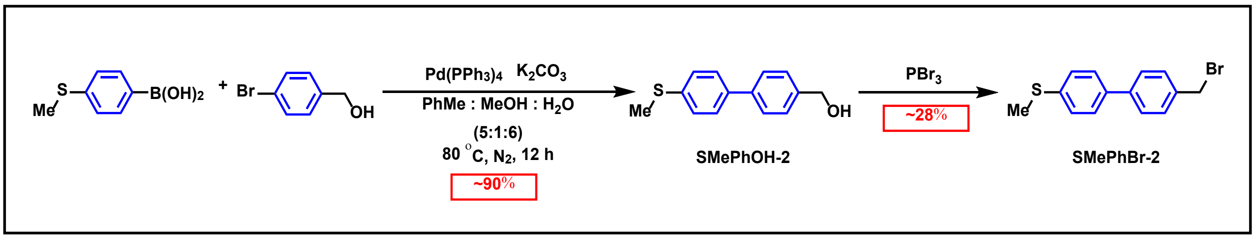

Scheme S2. Synthesis of **SMePhBr–2**.

SMePhOH–2: A 250 mL round-bottom flask, equipped with a magnetic stirrer, was charged with (4-(methylthio)phenyl)boronic acid (15 mmol, 1.0 equiv), (4-bromophenyl)methanol (18 mmol, 1.2 equiv) $Pd(PPh_3)_4$ (0.15 mmol, 0.01 equiv), K_2CO_3 (45 mmol, 3.0 equiv), toluene (75 mL), MeOH (15 mL) and H_2O (90 mL). The reaction mixture was stirred at 80 °C under an N_2 atmosphere for 12 h, cooled to room temperature, and passed through a pad of Celite. Then, 60 mL of water were added to the mixture and the solution extracted with ethyl acetate (60 mL × 3). The combined organic layers were washed with brine, dried over Na_2SO_4 and evaporated *in vacuo* to give the crude product **SMePhOH–2** as a white solid which was used for the next reaction without purification.

SMePhBr–2: To a solution of **SMePhOH–2** (8.6 mmol, 1.0 equiv) in dichloromethane (20 mL, 0.05 M) cooled at 0°C, PBr_3 (25.8 mmol, 3.0 equiv) was added. The mixture was stirred for 5 h at 0°C and then slowly allowed to warm up to RT over the following 10 h, cooled to room temperature. Then, 60 mL of ice water were added to the mixture and the solution extracted with dichloromethane (60 mL × 3). The combined organic layers were washed with brine, dried over Na_2SO_4 and evaporated *in vacuo*. The product was purified by silica gel chromatography using petroleum ether/dichloromethane (10:1) as the eluent to give **SMePhBr–2** as a white solid with a yield of 28%. ^{1}H NMR (600 MHz, Chloroform-*d*) δ 7.55 (d, J = 7.8 Hz, 2H), 7.51 (d, J = 7.9 Hz, 2H), 7.46 (d, J = 7.8 Hz, 2H), 7.32 (d, J = 8.1 Hz, 2H), 4.55 (s, 2H), 2.52 (s, 3H).

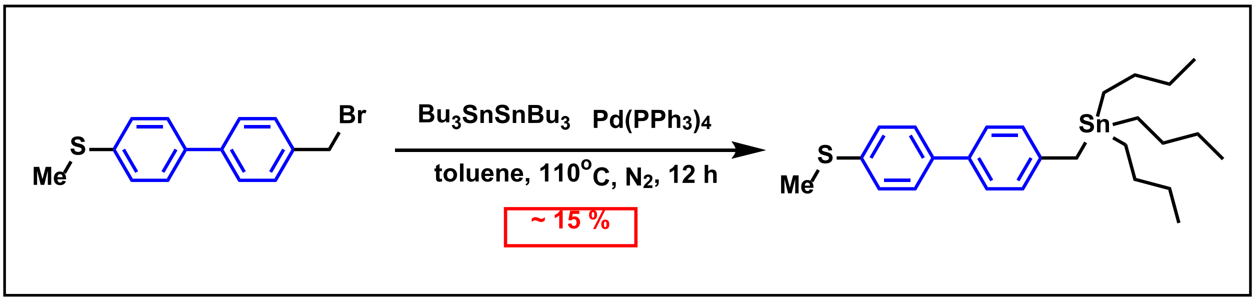

Supplementary Scheme 3 | Synthesis of **SMePhSn–2**.

SMePhSn–2: A 100 mL round-bottom flask, equipped with a magnetic stirrer, was charged with (4'-(bromomethyl)-[1,1'-biphenyl]-4-yl)(methyl)sulfane (2.3 mmol, 1.0 equiv), $Bu_3SnSnBu_3$ (2.6 mmol, 1.1 equiv), $Pd(PPh_3)_4$ (0.26 mmol, 0.1 equiv), toluene (60 mL). The reaction mixture was stirred at 110 °C under an N_2 atmosphere for 12 h, cooled to room temperature, and passed through a pad of Celite. Then, 60 mL of water were added to the mixture and the solution extracted with DCM (60 mL × 3). The combined organic layers were washed with brine, dried over Na_2SO_4 and evaporated *in vacuo*. The product was purified by silica gel chromatography using hexane as the eluent to give **SMePhSn–2** as as a yellow solid with a yield in ~15%. ^{1}H NMR (600 MHz, Chloroform-*d*) δ 7.49 (d, J = 8.3 Hz, 2H), 7.39 (d, J = 8.1 Hz, 2H), 7.30 (d, J = 8.4 Hz, 2H), 7.04 (d, J = 8.1 Hz, 2H), 2.51 (s, 3H), 2.34 (s, 2H), 1.47 – 1.36 (m, 6H), 1.26 (t, J = 7.4 Hz, 6H), 0.89 – 0.80 (m, 16H). ^{13}C NMR (151 MHz, Chloroform-*d*) δ 143.1, 138.4, 136.5, 135.0, 127.4, 127.2, 127.0, 126.6, 29.1, 29.0, 29.0, 27.5, 27.3, 27.1, 18.0, 16.2, 13.7, 9.4. HRMS (MALDI-TOF); calculated for **SMePhSn–2**: $[M\text{-}Bu]^+$ 448.1247, found 448.1244.

Section C. NMR Spectroscopy

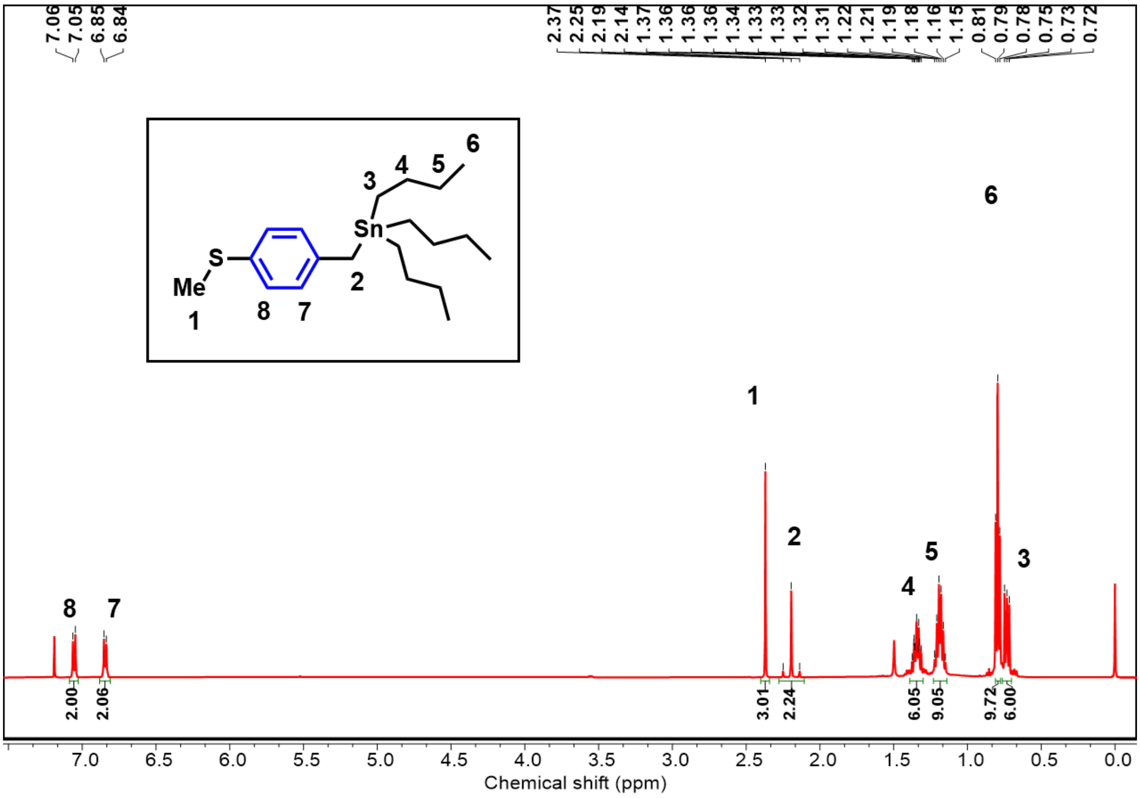

Fig. S1. ^{1}H NMR (500 MHz, Chloroform-*d*, 298 K) of **SMePhSn–1.**

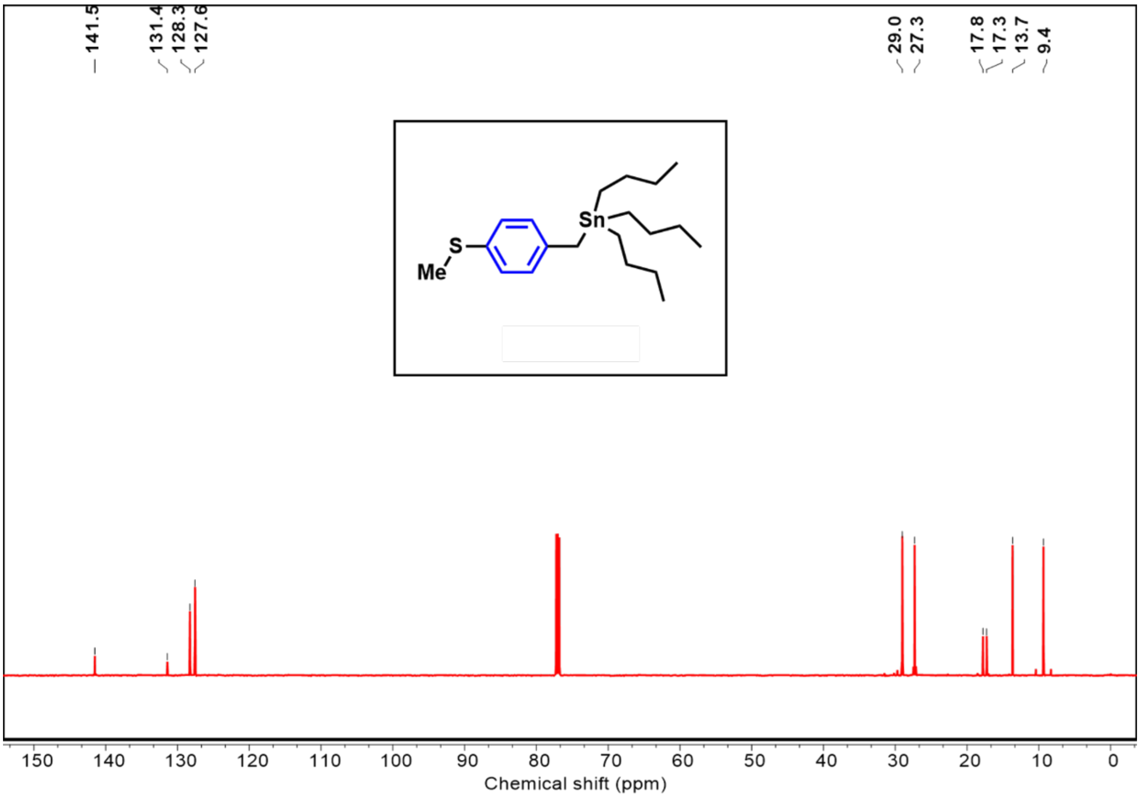

Fig. S2. ^{13}C NMR spectrum (126 MHz, Chloroform-*d*, 298 K) of **SMePhSn–1.**

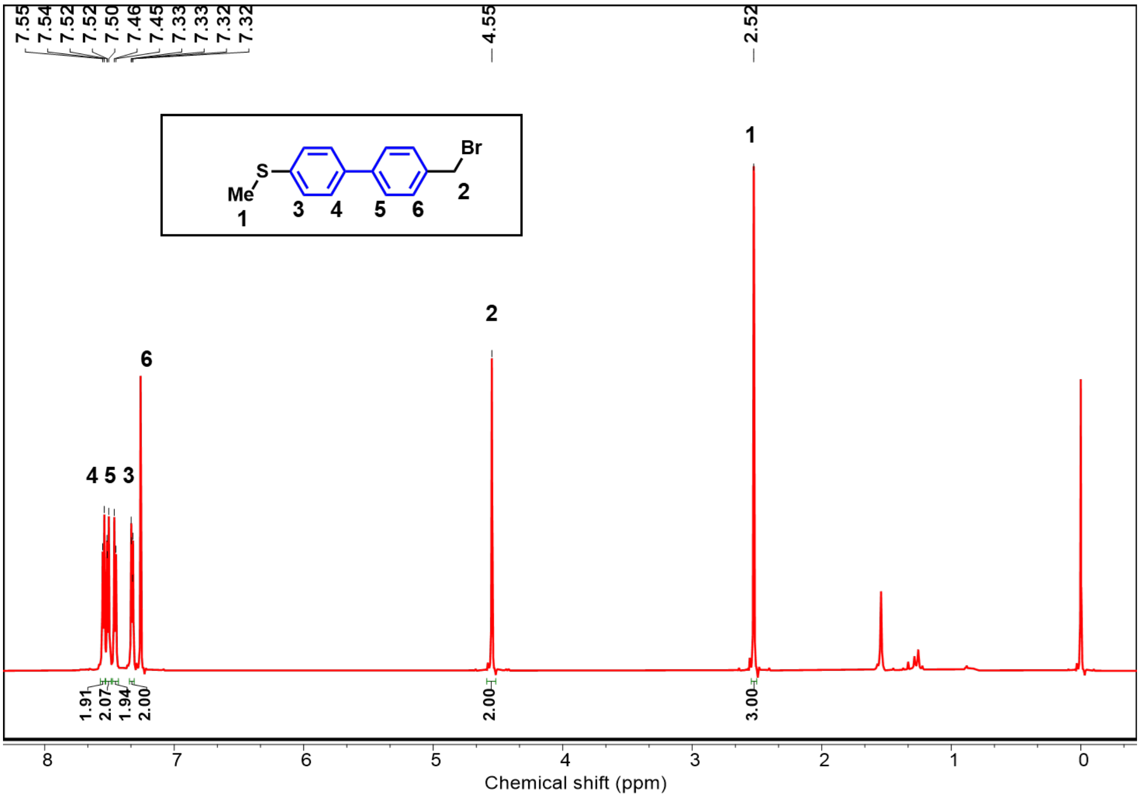

Fig. S3. ^{1}H NMR (600 MHz, Chloroform-*d*, 298 K) of **SMePhBr–2.**

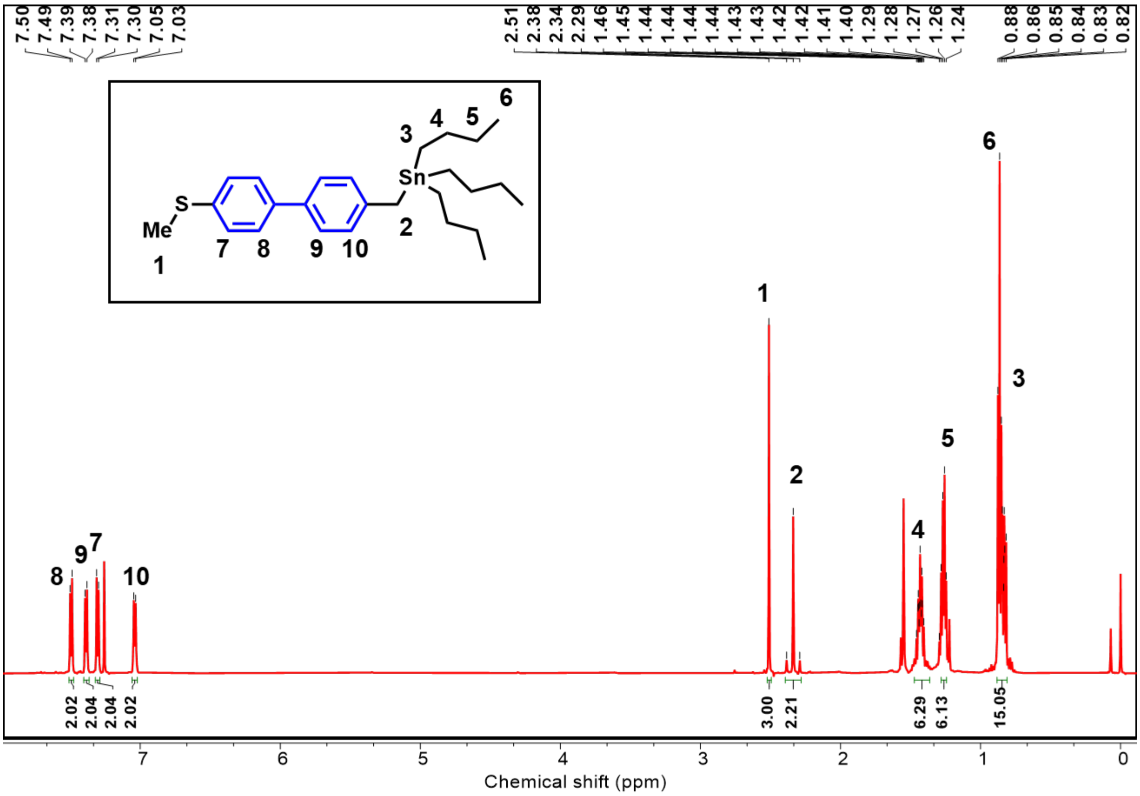

Fig. S4. ^{1}H NMR (600 MHz, Chloroform-*d*, 298 K) of **SMePhSn–2**.

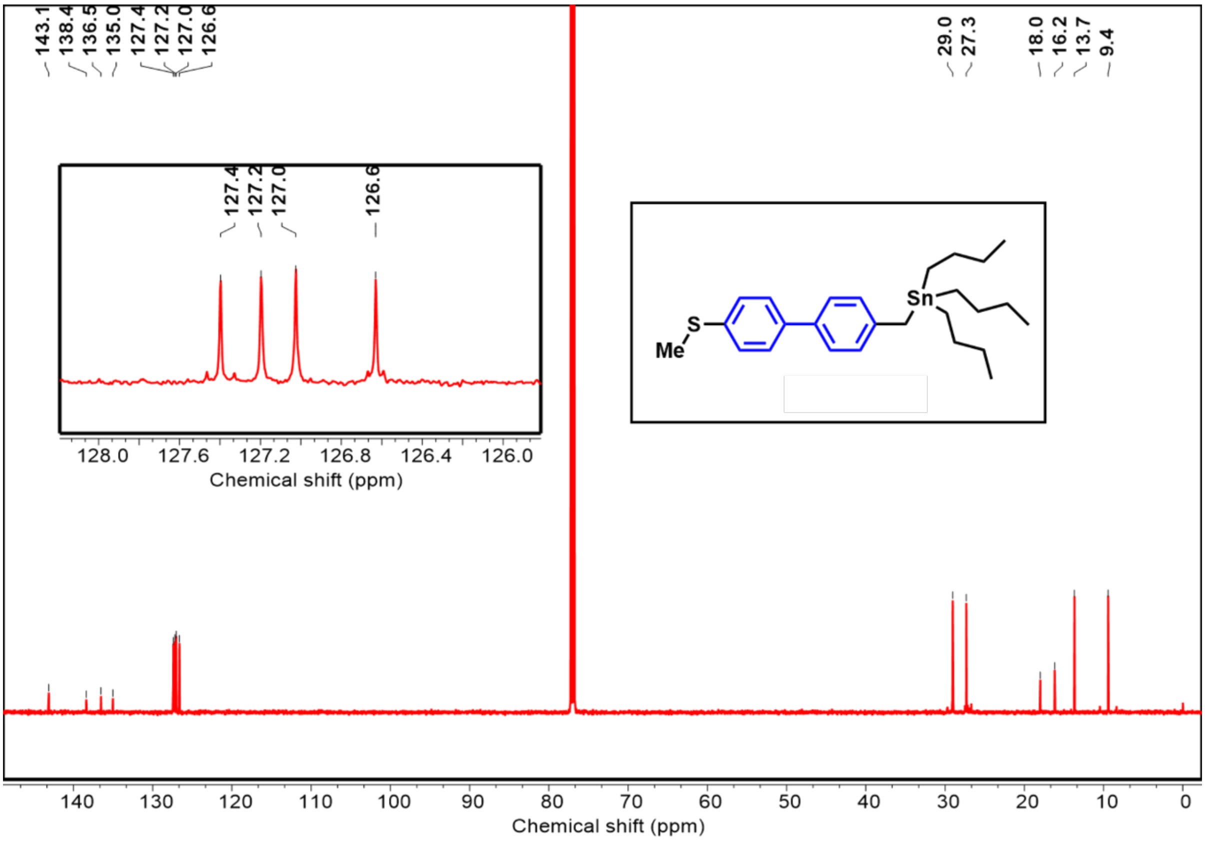

Fig. S5. ^{13}C NMR (151 MHz, Chloroform-*d*, 298 K) of **SMePhSn–2**.

Section D. Supplemental STM-BJ Measurements

STM-BJ Details. Scanning tunnelling microscope–based break junction (STM–BJ) measurements were performed (**Fig. S6**) using a custom-built STM that has been described[1] previously. In our experiment, the Au tips were prepared by electrochemical etching using Au wires with a diameter of 0.25 mm (99.998%, Beijing Jiaming Platinum Nonferrous Metals Co., Ltd). Subsequently, the Au substrates were prepared by depositing chromium (Cr)/Au layers with controlled thickness of 5/100 nanometers on a silicon substrate with 300-nm-thick SiO_2 layer (Suzhou Research Material Microtechnology Co., Ltd.). The conductance measurements were conducted at room temperature (20°C) under ambient conditions using 1,2,4-trichlorobenzene (TCB) as the solvent. When the connection between the Au tip and the substrate is broken, a new Au–Au atomic contact is established. A solution containing either target or control compounds at a concentration of 0.1 mM was prepared and 10 μL was dispensed onto the Au substrate using a pipette.

During the STM-BJ measurement, the positioning and movement of the Au tip are controlled by a motor and piezo. Firstly, the approximate position of the tip is controlled using a stepper motor (Harmonic Drive, LA-30B-10-F), allowing it to approach the substrate with an accuracy of less than 1 μm. Subsequently, the movement of the tip is controlled by a piezo stack (Thorlabs, PC4FL) operating at a speed of 20 nm/s. With a maximum driving voltage of ±10 V, the piezo stack can precisely control the displacement of the tip, which is approximately 4.6 μm with a variation range of ±15%. In order to ensure proper feedback control for conductance measurements, upper and lower limits of the current are defined. This feedback control mechanism is essential for maintaining the current within the desired range. As the tip moves upward, an Au–Au atomic contact is established between the tip and the substrate. Subsequently, the tip is further pulled, leading to the rupture of the contact. This action brings the target compounds in the nanogap into contact with the tip and the substrate, forming a single-molecule junction in which the conductance of the molecule is measured. Further pulling of the tip breaks the connection between the molecule and electrodes, causing the current to drop below the limit (1 pA) and become undetectable by the current amplifier. Throughout the entire process of contact rupture and reconnection, the bias is adjusted from 0.1 to 0.7 V. Real-time conductance is recorded using a customized *I*–*V* converter capable of sampling the conductance at a rate of 20 kHz.

Data Analysis. In order to determine the most probable conductance and stretching distance during the measurements of single-molecule conductance, thousands of individual breaking traces were collected. A statistical approach without any data selection was employed for analysis. In order to construct one-dimensional (1D) and two-dimensional (2D) conductance-displacement histograms, all individual traces were collected with a bin size of 1100 for

$\log(G/G_0)$ ranging from –10 to +1, and a bin size of 1000 for Δz ranging from –0.5 to 3 nm. The peak shift was determined using Gaussian fitting, which represents the most probable molecular conductance. The 2D conductance-displacement histograms were generated by aligning with a relative zero point ($\Delta z = 0$) at 0.5 G_0. The relative stretching distance (Δz) was determined from the position where the conductance is 0.5 G_0 to the molecular conductance region just before the end of the molecular plateau. The peak in the histogram signifies the most probable length of the plateau. In order to calculate the absolute displacement (z^*), which correlates with the most probable length of the molecular junction, the relative displacements were adjusted by adding the snap-back distance (Δz_{corr}) to the relative displacement (Δz), specifically, $z^* = \Delta z + \Delta z_{\text{corr}}$. Based on previous findings, Δz_{corr} was experimentally determined to be 0.5 ± 0.1 nm[2].

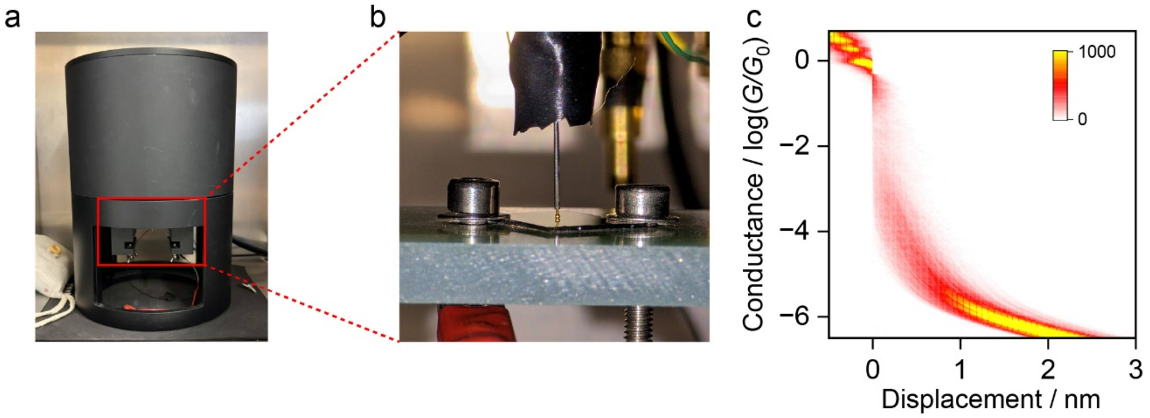

Fig. S6. The home-built STM-BJ set-up. a, Photographs of the home-built STM set-up. **b**, An enlarged area of the tip and substrate. **c,** 2D Conductance-displacement histograms of control experiments illustrate the background current on a clean Au substrate without targeted compounds.

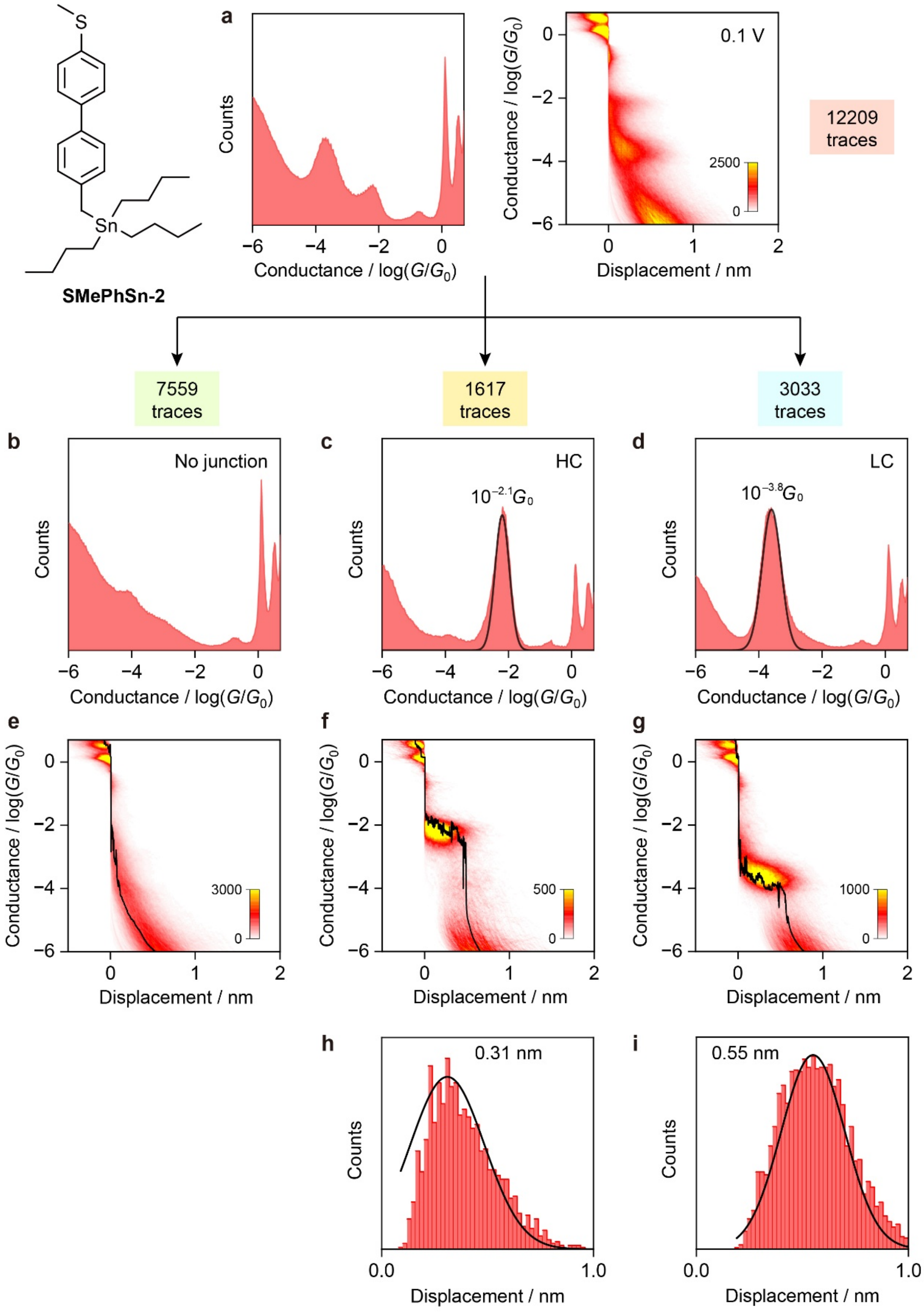

Fig. S7. Conductance measurements and cluster analysis of SMePhSn–2 (0.1 mM in TCB) under a 0.1 V bias. a, Time-dependent 1D and 2D conductance histograms of **SMePhSn–2** measured at 0.1 V bias. **b–d**, 1D conductance histograms of three clusters (No junction, HC, and LC) identified by machine learning-based clustering analysis. **e–g**, Corresponding 2D histograms and representative single-molecule conductance traces for each cluster. **h–j**, Distributions of conductance step lengths for HC and LC, respectively.

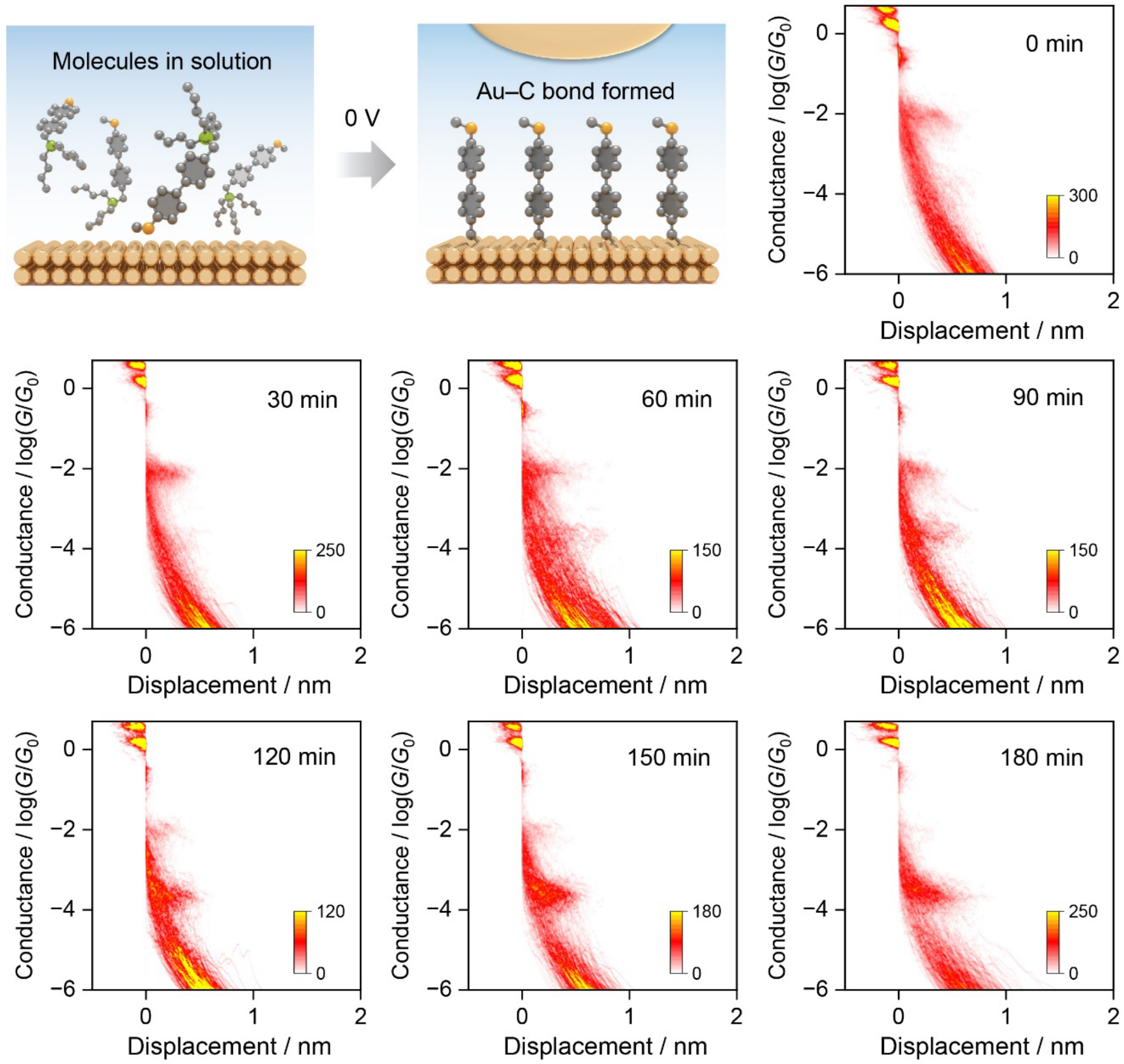

Fig. S8. Time-dependent 2D conductance histograms showing the assembly process of **SMePhSn–2** without EEF.

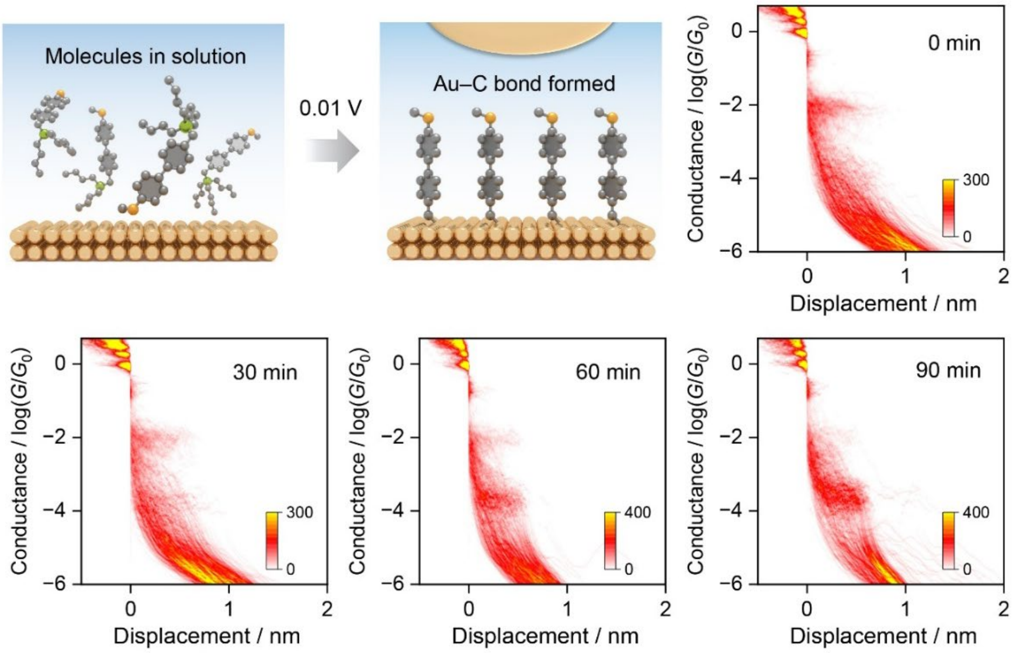

Fig. S9. Time-dependent 2D conductance histograms showing the assembly process of **SMePhSn–2** with EEF strength of 10^7 V/m.

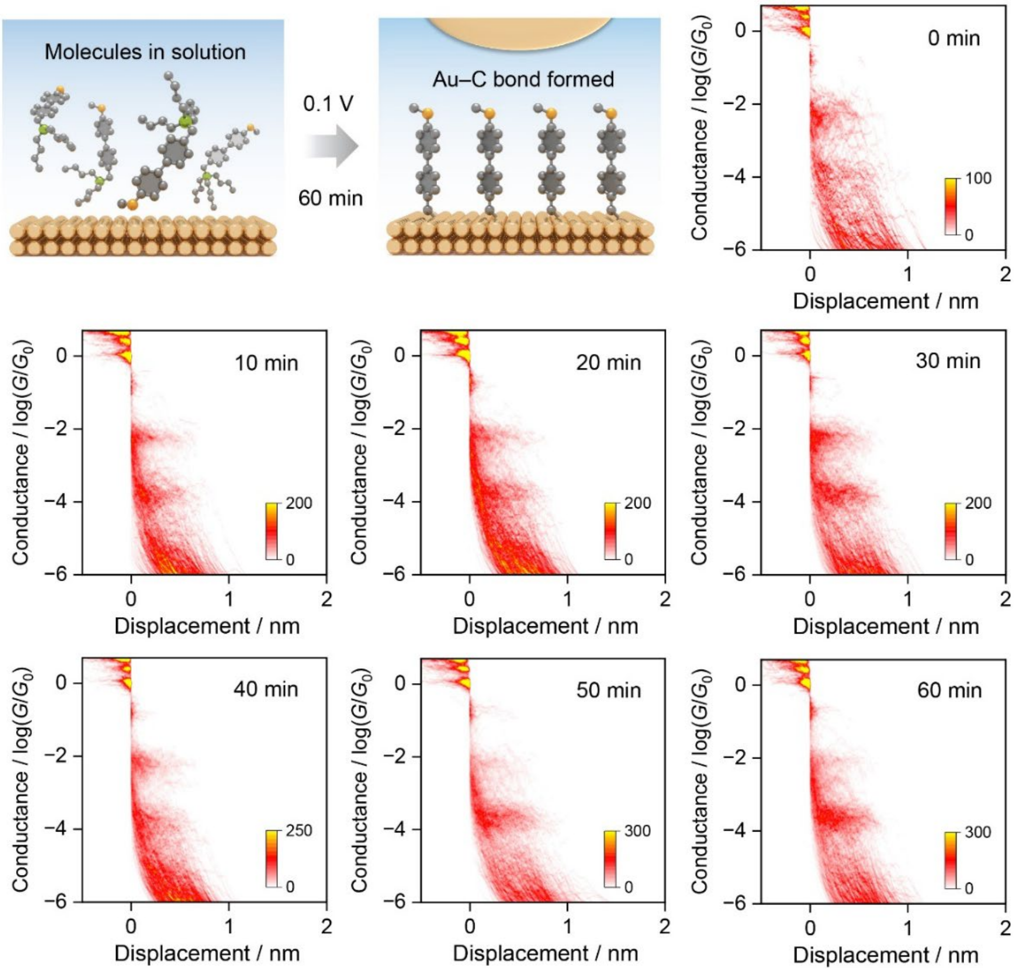

Fig. S10. Time-dependent 2D conductance histograms showing the assembly process of **SMePhSn–2** with EEF strength of 10^8 V/m.

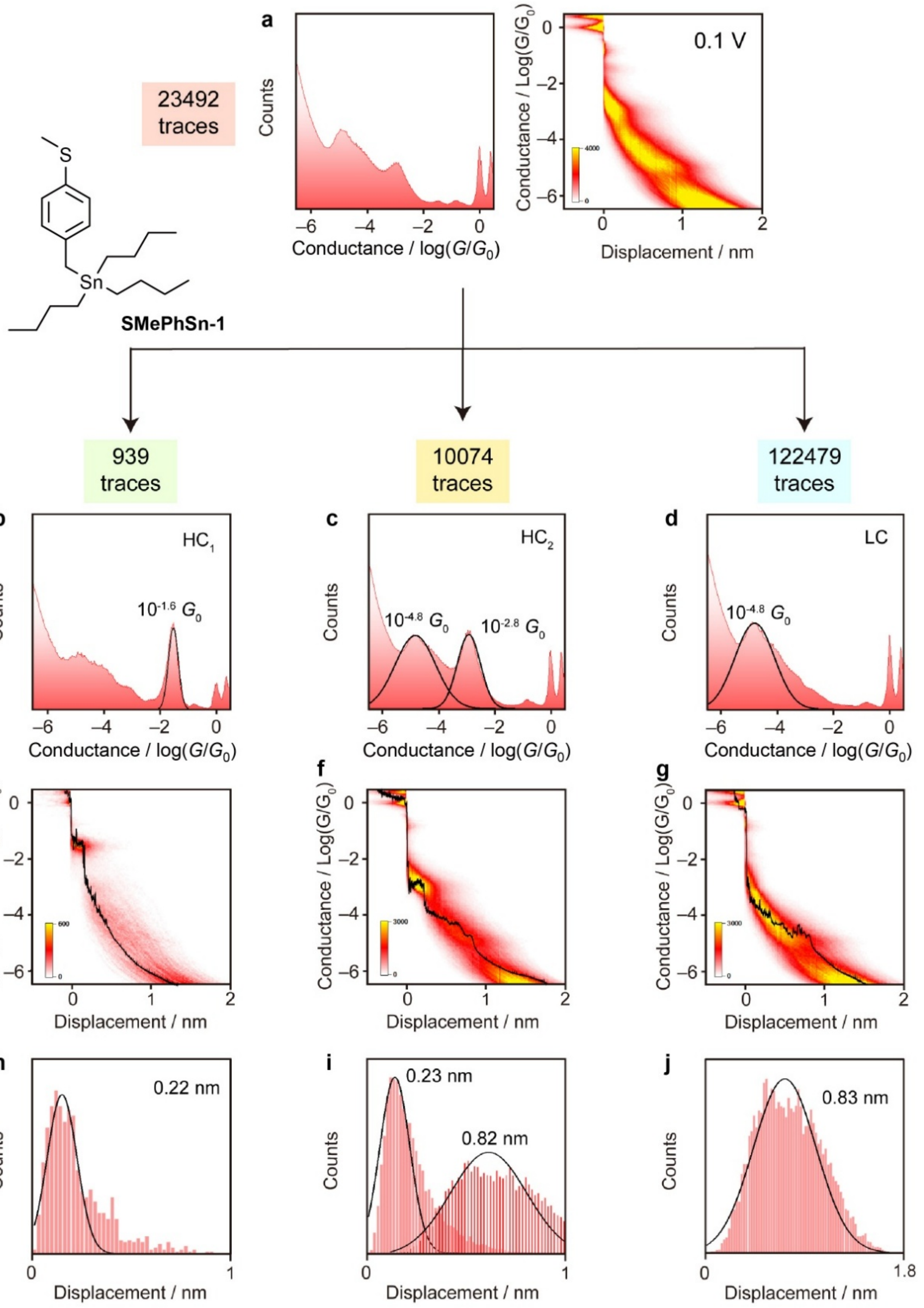

Fig. S11. Conductance measurements and cluster analysis of SMePhSn–1 (0.1 mM in TCB) under a 0.1 V bias. a, Time-dependent 1D and 2D conductance histograms of **SMePhSn–1** measured at 0.1 V bias. **b–d**, 1D conductance histograms of three clusters (HC_1, HC_2, and LC) identified by machine learning-based clustering analysis. **e–g**, Corresponding 2D histograms and representative single-molecule conductance traces for each cluster. h–j, Distributions of conductance step lengths for HC_1, HC_2, and LC, respectively.

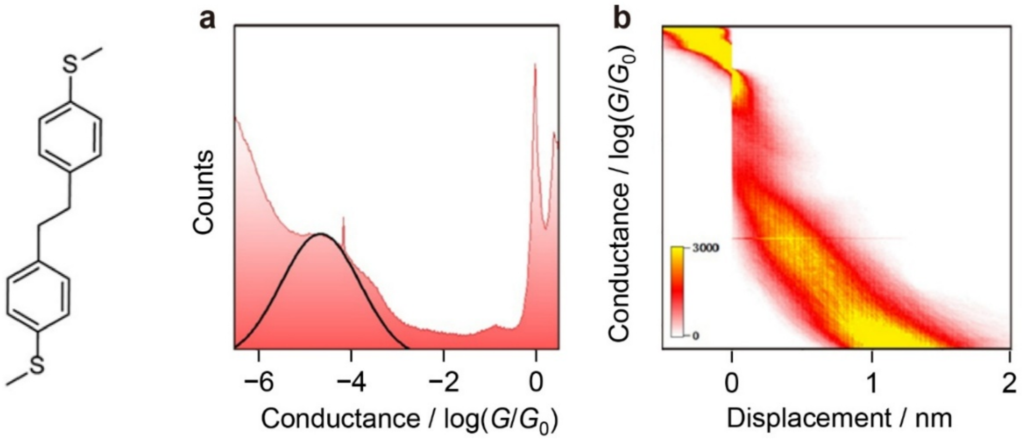

Fig. S12. Conductance measurements of radical coupling dimer product (0.1mM in TCB) from SMePhSn–1 at a 0.1 V bias. a, 1D conductance histogram. **b**, 2D conductance histogram.

Section E. Theoretical calculations

DFT Calculations. Firstly, the structural optimization of **SMePhSn–*n*** were carried out using B3LYP-D3/6-311G(d,p) basis set in the Gaussian 16 package. The structural optimization of Au–**SMePhSn–*n*** including Au–C covalent bonds were carried out using MO6L/Def2SVP basis set in the Gaussian 16 package. Secondly, the optimized molecular structures were then bridged between two Au electrodes to construct the single-molecule devices. In order to build devices containing the Au–molecule–Au sandwich model, the surface of the Au electrodes was shaped into a pyramidal configuration. The top Au atom was coordinated by the terminal S atom of the molecule, while the bottom Au atom was coordinated by covalently bonded with C atom (**Fig. S13)**. Thirdly, we conducted geometric optimization for the devices by allowing relaxation in distances between all atoms within the bridge molecules as well as those between top and bottom Au electrodes. In order to expedite calculations, the scattering and extension area of the electrodes are maintained rigid, with the emphasis placed on optimizing the adsorption configuration between the electrodes and the anchoring groups. The geometry optimization and transmission spectra calculation of the devices were implemented in Quantum ATK Q-2022.03 software. We adopted the generalized gradient approximation (GGA) Perdew-Burke-Ernzerhof (PBE) exchange-correlation functional, Fritz-Haber-Institute (FHI) pseudopotential combined with single zeta polarized group for Au atoms, and Fritz-Haber-Institute pseudopotential combined with double zeta polarized group for other atoms.

The transmission coefficient $T(E)$ describing the probability that electrons at energy E propagate from the left electrode to the right electrode was calculated using Gollum code[3].

which combines the average field Hamiltonian and the overlap matrix with the quantum transfer theory based on Landauer, using the expression:

$$T(E) = \mathrm{tr}[T_L(E)G^R(E)\mathit{\Gamma}_\mathrm{R}(E)G^A(E)] \tag{S8}$$

where $\mathit{\Gamma}_\mathrm{L,R}(E) = i(\Sigma_\mathrm{L,R}(E) - \Sigma_\mathrm{L,R}{}^\dagger(E))/2$, $G_r(E) = \left(g^{-1} - \Sigma_\mathrm{L} - \Sigma_\mathrm{R}\right)^{-1}$ and g is the Green's function of the isolated molecule. $\mathit{\Gamma}_\mathrm{L,R}$ determines the widths of transmission resonances, $\Sigma_\mathrm{L}(E)$ $(\Sigma_\mathrm{R}(E))$ are the self-energies describing the contact between the molecule and left (L) (right (R)) electrode, and $G^R(G^A)$ is the retarded Green's function of the molecule in the low temperature conductance and evaluated by the following formula:

$$G = G_0 T(E_\mathrm{F}) \tag{S9}$$

where $G_0 = 2e^2/h$ is the conductance quantum number, h is Planck's constant, and e is the elementary charge.

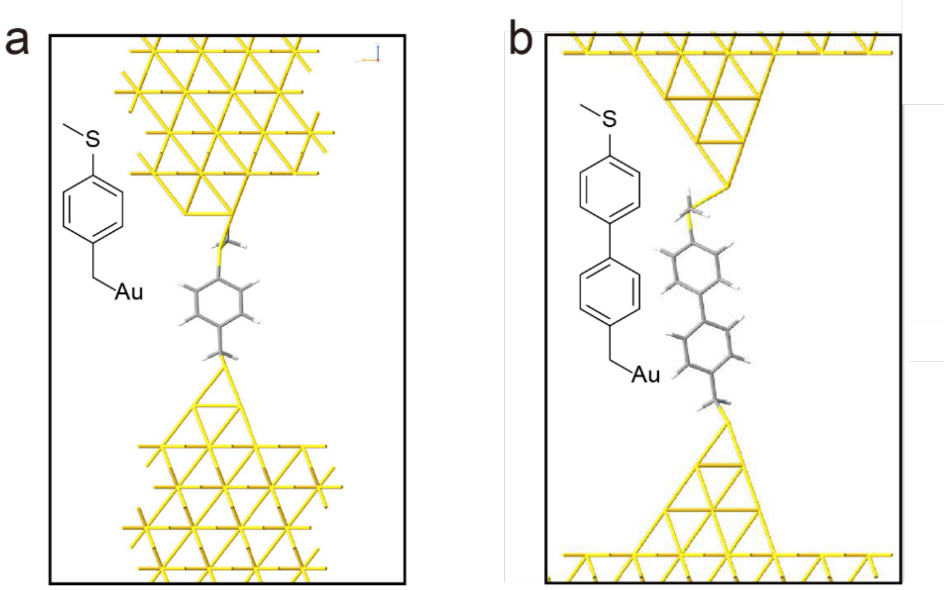

Fig. S13. Optimized junction geometries for **a,** Au–**S-Ph^1-C**–Au junction, **b,** Au–**S-Ph^2-C**–Au junction demonstrate Au top electrodes binding to thiolmethyl anchors and bottom electrodes binding to C atom forming Au–C covalent contacts.

Section F. Supplemental References

1. V. Kaliginedi, P. Moreno-Garcia, H. Valkenier, W. Hong, V. M. Garcia-Suarez, P. Buiter, J. L. Otten, J. C. Hummelen, C. J. Lambert and T. Wandlowski, Correlations between molecular structure and single–junction conductance: a case study with oligo(phenylene-ethynylene)–type wires, *J. Am. Chem. Soc.*, **2012**, *134*, 5262–5275.
2. D. Z. Manrique, C. Huang, M. Baghernejad, X. Zhao, O. A. Al-Owaedi, H. Sadeghi, V. Kaliginedi, W. Hong, M. Gulcur, T. Wandlowski, M. R. Bryce and C. J. Lambert, A quantum circuit rule for interference effects in single-molecule electrical junctions, *Nat. Commun.*, **2015**, *6*, 6389.
3. J. Ferrer, C. J. Lambert, V. M. García-Suárez, D. Z. Manrique, D. Visontai, L. Oroszlany, R. Rodríguez-Ferradás, I. Grace, S. W. D. Bailey, K. Gillemot, H. Sadeghi and L. A. Algharagholy, GOLLUM: A next-generation simulation tool for electron, thermal and spin transport, *New J. Phys.*, **2014**, *16*, 093029.